Rosette-scan video-rate atomic force microscopy: Trajectory patterning and control design

View Online   Export Citation   CrossMark

Nastaran Nikooienejad,[a] (iD) Mohammad Maroufi,[b] (iD) and S. O. Reza Moheimani[c] (iD)

AFFILIATIONS

Erik Jonsson School of Engineering and Computer Science at the University of Texas at Dallas, Richardson, Texas 75080, USA

[a] Electronic mail: nastaran.nikooienejad@utdallas.edu
[b] Electronic mail: mohammad.maroufi@utdallas.edu
[c] Author to whom correspondence should be addressed: reza.moheimani@utdallas.edu

ABSTRACT

We present an analysis and a systematic design methodology for a novel nonraster scan method based on a rosette pattern and demonstrate its application in video-rate atomic force microscopy. This pattern is traced when the lateral axes of a parallel kinematic scanner are commanded to follow a combination of two sinusoids with identical amplitudes and different frequencies. We design an internal-model-based controller to enhance the tracking performance of this pattern and implement the scheme on a microelectromechanical system scanner. The results reveal high-precision tracking of the rosette pattern in order to acquire time-lapsed atomic force microscope images at the rate of 10 frames/s.

Published under license by AIP Publishing. https://doi.org/10.1063/1.5098499

I. INTRODUCTION

The atomic force microscope (AFM) is widely used in science and technology for interrogation and manipulation of matter at the nanoscale.[1–4] The traditional method of scanning in AFM is based on rastering in which one lateral axis of the positioner is made to follow a triangular or sawtooth signal, while the other axis follows a ramp or staircase setpoint. Data are collected over a grid as the positioner sweeps the imaging area with constant linear tip velocity.[5] Due to the infinite number of harmonics in the triangular wave,[6] the functionality of this method is only satisfactory at low-speed scans. Even though several approaches have been developed to improve the tracking performance of raster scanning,[5,7] achieving acceptable responses in video-rate imaging becomes quite challenging.

To overcome the scan speed restrictions inherent to rastering, nonraster scan methods such as spiral,[8–10] Lissajous,[11,12] and cycloid[13,14] scan patterns have been proposed to enable high-speed imaging in AFM. Tracking harmonic waveforms that produce these nonraster patterns requires far less bandwidth compared with rastering, and this enables much higher scan speeds.

To implement each nonraster scan method, a number of issues need to be addressed. For example, a constant angular velocity (CAV) spiral can be generated by commanding the lateral axes of a scanner to follow sine and cosine waves with identical frequencies and slowly increasing amplitudes.[9,15] Alternatively, to trace a constant linear velocity (CLV) spiral, the frequency and amplitude of the sinusoidal setpoints are varying simultaneously.[15,16] Although the linear speed of the AFM probe tip in a CLV spiral trajectory is constant leading to a great homogeneity of data distribution, the scan frequency approaches infinity at the image center complicating the accurate tracking of this pattern. In a CAV spiral, on the other hand, the linear tip velocity increases in tune with the radius of the scan, leading to the requirement for a very high-bandwidth z-axis nanopositioner, if video-rate AFM imaging is the ultimate goal. To overcome these constraints, an optimal spiral trajectory is proposed in Ref. 16 that combines the advantages of both CAV and CLV spirals.

Cycloid and Lissajous trajectories are two other patterns used in nonraster scan atomic force microscopy. The cycloid pattern gradually moves forward with a fixed pitch, making it suitable for tracking stringlike samples such as the DNA.[17] To generate this pattern, one axis of the nanopositioner follows a cosine wave, while the other axis tracks a sine wave superimposed on a ramp signal. In the Lissajous trajectory, on the other hand, the in-plane axes of the nanopositioner are driven by pure sinusoids with constant amplitudes. A slight difference between the phase and frequency of sinusoids can generate various Lissajous patterns with rectangular-shaped scan areas. Lissajous is a self-repeating pattern and can be employed in sequential

scanning. However, this scan pattern traverses the entire scan area in a half period and repeats itself in reverse during the second half period.[11] Therefore, the tip experiences opposite velocities in two consecutive frames. Moreover, in the Lissajous pattern, the largest distance between two scan lines occurs at the center of scan area,[11] meaning that Lissajous fails to prioritize the features at the center.

In this paper, we propose a new nonraster scan method. The idea is to design and implement a smooth trajectory whereby sequential AFM imaging can be performed continuously without the need for a high-bandwidth tracking controller. Nonraster scans based on cycloid and spiral patterns must be performed in a sequential manner for video-rate imaging, meaning that the nanopositioner is required to alternately move forward/outward and backward/inward to produce multiple frames.[14] This type of motion can induce large tracking errors due to the sharp transitions at the edge of scan area. The scan trajectory proposed here, however, does not require back and forth motions to achieve sequential scanning. The proposed pattern intersects itself at specific points creating curvilinear rhombus interstices. These self-intersections of large temporal separation provide information that may be used to detect and remove height drift in AFM images in a manner similar to Ref. [18].

In the remainder of the paper, we present a rigorous mathematical analysis of the nonraster pattern and derive closed-form formulas to determine the scan time and resolution. In addition, we state a step-by-step procedure for designing the pattern based on the desired scan parameters. We use a two degree-of-freedom (2-DOF) microelectromechanical system (MEMS) nanopositioner[19] together with damping and internal-model-based feedback controllers to implement this nonraster method and achieve video-rate AFM scans at the rate of 10 frames per second (fps).

II. THE ROSETTE PATTERN

Among the closed plane curves, hypotrochoids and epitrochoids belong to the large family of roulettes.[20] When the centers of two tangent circles are located on the same side of a common tangent line and one circle remains fixed with the second circle rolling around the first, a point on the diameter of the rolling circle traces a hypotrochoid. If both centers are on opposite sides, a point on the diameter of the rolling circle traces an epitrochoid.[21] A rosette is an epitrochoid where the distance between the center of the rolling circle and the rotating point is equal to the sum of the radii of the fixed and rolling circles. Assuming a circular-shaped area with a radius of R, a rosette pattern can be generated when the x and y axes are made to trace the following set points:

$$x = R\cos(n\theta)\cos(\theta),$$
$$y = R\cos(n\theta)\sin(\theta). \quad (1)$$

Here, $\theta = 2\pi f t$ determines the angle and f is the fundamental scan frequency, which determines the scanning time. In general, n can be selected as an integer, rational, or irrational number which leads to distinct rosette shapes as shown in Fig. 1. The number of petals in a rosette pattern depends on n. For instance, a rosette has 4 petals with $n = 2$ and 8 petals if $n = 0.8$. However, selecting an irrational n results in an infinite number of petals as shown in Fig. 1(d). To ensure that the rosette pattern can cover the entire circular scan area
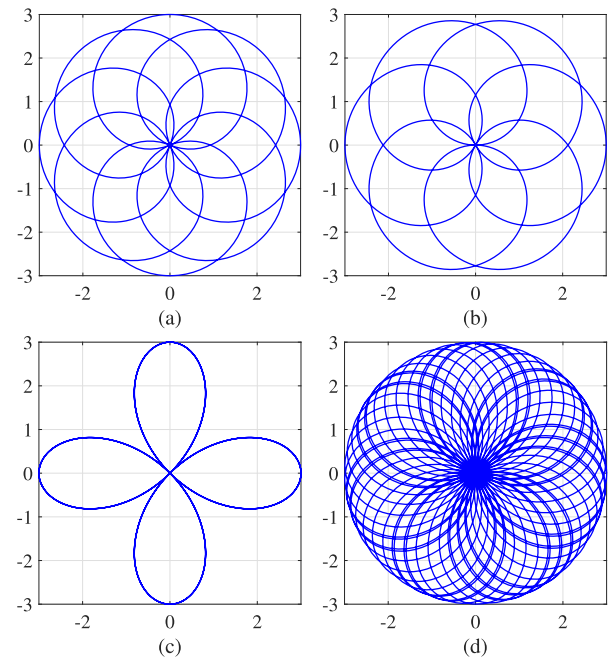

FIG. 1. Rosette patterns with (a) $n = 4/5$, (b) $n = 3/4$, (c) $n = 2$, and (d) $n = \sqrt{2}$.

with a definite number of petals, we choose n as the rational number,

$$n = \frac{N}{N+1}, \qquad N \in \{2, 4, \ldots, 2k, \ldots\}. \quad (2)$$

Here, N is an even integer. For small odd values of N, the rosette pattern does not reach the top and bottom boundaries of the scan window as shown in Fig. 1(b). For large values of N, however, there is no significant difference between the rosettes with odd or even values of N.

A. Analysis of the rosette pattern

In this subsection, we present a detailed analysis of the rosette pattern resulting in a closed-form expression for the scan resolution. According to Eq. (1), x and y reference signals can each be expressed as the sum of two sinusoids as

$$x = \frac{R}{2}\left\{\cos[(1+n)\theta] + \cos[(1-n)\theta]\right\},$$
$$y = \frac{R}{2}\left\{\sin[(1+n)\theta] + \sin[(1-n)\theta]\right\}. \quad (3)$$

Therefore, the reference signal of each axis contains a high frequency sinusoid superimposed on a low frequency one and the reference frequencies can be determined from

$$f_1 = (1+n)f,$$
$$f_2 = (1-n)f. \quad (4)$$

The rosette is a periodic pattern because it repeats itself over a certain time interval. In Appendix A, we show that x and y have identical periods and the pattern period (T) is the least common multiple
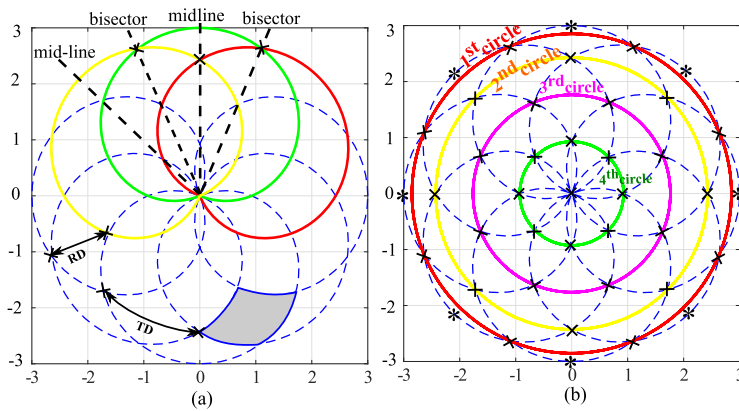
FIG. 2. (a) Three successive petals in a rosette pattern are shown by different colors. The tangential distance (TD) and radial distance (RD) in a rosette pattern generate a curvilinear rhombus (colored in gray). (b) Concentric circles crossing the intersections in a rosette pattern with $R = 3$ μm, $N = 4$, and $T = 1$ s. The intersections and edge points are shown by $\times$ and $*$, respectively.

(LCM) of all individual periods of the reference terms, i.e.,

$$T = \frac{N+1}{f}. \tag{5}$$

As shown in Fig. 1, the number of petals depends on the value of n. Since n is selected as a rational number in Eq. (2), the number of petals in the proposed scan pattern is $2N$; see Appendix B. The pattern symmetry indicates that the petals intersect not only at the origin but also at their midlines as well as at the bisector of two consecutive midlines.[21] The number of midlines or bisectors is similar to the number of petals in the pattern. Figure 2(a) shows the intersections of three successive petals along with their midlines and bisectors. In the rosette pattern, the intersections lie on N concentric circles as depicted in Fig. 2(b). The intersections that are close to the periphery are located on the first circle, and the ones close to the origin remain on the Nth circle. Apart from the intersections at the center of the pattern, the scan lines intersect $2N^2$ times in a rosette pattern.

To determine the radius of each concentric circle, the smallest polar angle where the first crossing point occurs at the corresponding circle can be obtained as

$$\theta_i = i\pi\left(1 + \frac{1}{2N}\right), \qquad i \in \{1, 2, \ldots, N\}. \tag{6}$$

As shown in Fig. 3, θ_1 to θ_4 contribute to the polar angles of the first crossing points laid on different concentric circles. As is clear,

θ_1 to θ_4 alternately determine the bisectors and midlines of petals in the pattern. Therefore, knowing θ_i enables us to obtain the radius of each concentric circle using Eq. (1), as follows:

$$r_i = R\cos(n\theta_i), \qquad i \in \{1, 2, \ldots, N\}. \tag{7}$$

With the radius of concentric circles known, we can determine the in-plane imaging resolution. The scan resolution can be defined as the largest distance between two nearby scan lines. This definition is valid provided that the sampling frequency is high enough so that the distance between two successive sampled points remains much smaller than the distance between scan lines. To obtain a measure for resolution, we seek the largest square-shaped area in the pattern which encompasses no data point. To do this, we first need to define the tangential distance (TD) and the radial distance (RD) between two crossing points shown in Fig. 2(a). TD is the arc length between two consecutive crossing points on a circle and is determined by the radius of the circle and the angle between the crossing points. Therefore, this distance is similar for all the crossing points lying on the same circle. The minimum value of TD occurs around the origin and increases to its maximum value at the largest circle close to the periphery of the pattern. The radial distances (RD), on the other hand, are categorized into two classes. The first one is the distance between every other consecutive circles, and the second is the radii of the last two concentric circles around the origin. We acquire RD and TD as
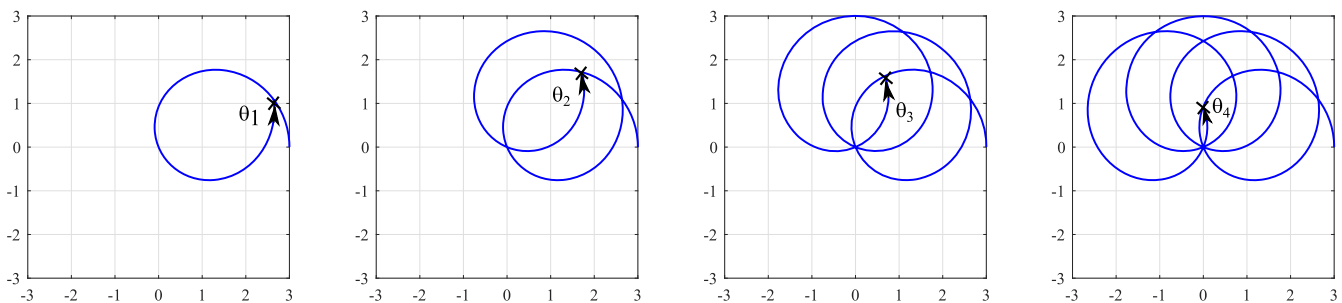

FIG. 3. Smallest polar angles θ_1 to θ_4 which determine the first intersections on the concentric circles in a rosette pattern with $R = 3$ μm and $N = 4$.

$$RD_{k+1} = r_k - r_{k+2}, \quad k = 0, \ldots, N,$$
$$TD_{k+1} = r_{k+1}\left(\frac{\pi}{N}\right), \tag{8}$$

where r_k denotes the radius of the kth concentric circle in the pattern, $r_0 = R$, and $r_{k>N} = 0$. As shown in Fig. 2(a), the crossing points form a curvilinear rhombus, with TD and RD being the diagonals. The area of rhombus varies as we move away from the origin. The maximum area occurs on the central concentric circles and decreases symmetrically toward either sides. Therefore, the largest area and, consequently, the image resolution can be obtained by finding the rhombus with the largest area in the pattern. Here, the distance between two adjacent scan lines is also maximum. In Appendix C, we show that the largest area occurs at the two central circles, i.e., $k = \{(N/2), (N/2) + 1\}$, and the resolution can be expressed by

$$P \approx \frac{R\pi}{2N}. \tag{9}$$

Note that in our previous work,[22] the rosette resolution was introduced as the largest distance between the crossing points occurred on the outermost concentric circle leading to a resolution twice of P. This definition leads to excessive data points accumulated at the peripheries with minimal contribution to the image quality over the scan area.

To create an image of nonraster sampled data, an interpolation technique such as the Delaunay triangulation is employed.[23] In this method, the scan area is subdivided into small triangles with vertices obtained from the sampled data to generate a triangular mesh; then, the height of unknown data points is approximated from the known data points to create a 3D image. For instance, Fig. 4 shows a rosette pattern sampled data and its 2D Delaunay triangulation. We observe that the largest triangles are located on the central concentric circles of the rosette pattern which aligns with our definition of resolution.

B. Properties of the rosette pattern

The rosette pattern is highly suitable for sequential scanning of circular-shaped areas because it allows AFM imaging to be
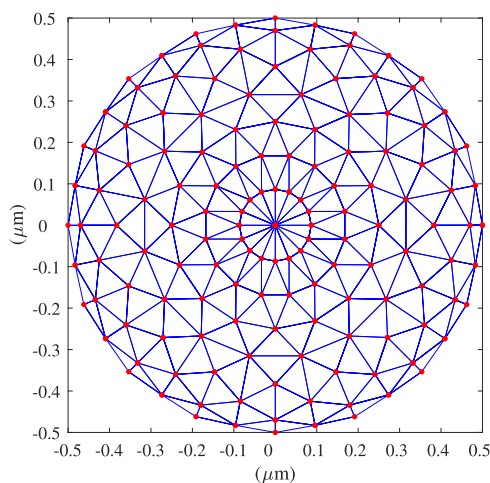

FIG. 4. Rosette sampled points (red dots) and Delaunay triangles (blue triangles). $R = 0.5\ \mu m$, $P \approx 100$ nm, $T = 1$ s, and $f_s = 288$ Hz.

performed continuously without the usual requirement for a high-bandwidth tracking controller. Furthermore, tracking of this scan pattern is straightforward and intuitive since the reference signals are harmonic waveforms.

Considering the reference signals in Eq. (3), the linear tip velocity, $v = \sqrt{\dot{x}^2 + \dot{y}^2}$, is obtained as

$$v = 2\pi Rf\sqrt{1 + (n^2 - 1)\sin^2(2\pi nft)}. \tag{10}$$

According to Eqs. (2) and (9), for high-resolution AFM imaging with the rosette pattern, N becomes large, while n approaches unity. Hence, $(n^2 - 1)\sin^2(2\pi nft) \ll 1$ and the tip velocity in Eq. (10) can be approximated by

$$v \simeq 2\pi Rf. \tag{11}$$

We observe that the linear tip velocity is approximately constant throughout a scan. Using Eq. (10) and knowing $n < 1$, the maximum tip velocity is obtained as $v_{max} = 2\pi Rf$ when $\sin(2\pi nft) = 0$. Figure 5(a) shows the absolute linear tip velocity at 10 fps. A slight velocity deviation (about 0.5%) is observable in this pattern. Figure 5(b) presents the tip velocity variation as a function of the number of concentric circles (N). Clearly, the tip velocity variation is negligible for larger values of N.

The maximum tip velocity is one of the factors which determines the required bandwidth of the z-axis nanopositioner in AFM
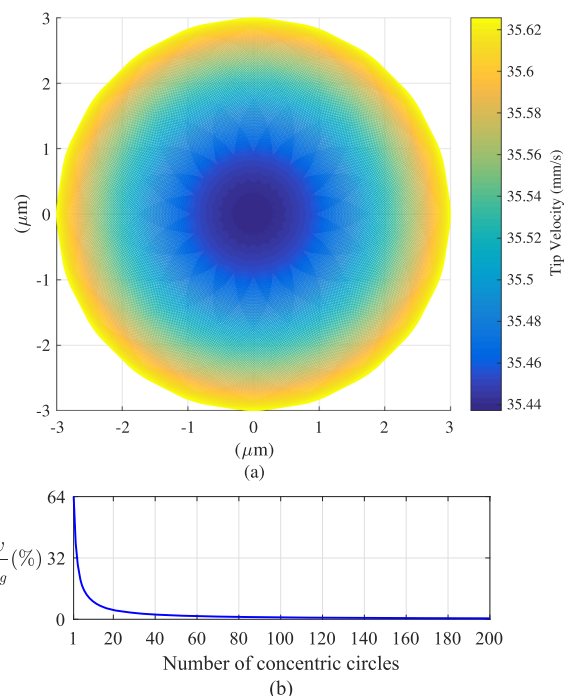

FIG. 5. (a) Tip velocity of a rosette pattern when $R = 3\ \mu m$, $P = 25$ nm, and the scan time is 0.1 s. (b) Variation of velocity in a rosette pattern with different numbers of concentric circles (N). Here, $\Delta v = v_{max} - v_{min}$ and v_{avg} denotes the average tip velocity.

TABLE I. The scan frequency and maximum tip velocity for rosette, Lissajous, CAV spiral, cycloid, and raster methods considering fixed scan area, resolution, and scan time.

Scanning method	Scan frequency (Hz)	Maximum velocity (mm/s)
Rosette	$f_1 = 3770$ $f_2 = 10$	35.62
Lissajous[11]	$f_x = 2360$ $f_y = 2355$	55.69
CAV spiral[16]	1190	22.62
Cycloid[14]	1610	20.17
Raster[24]	2127	22.62

imaging. Table I compares the maximum tip velocity and the corresponding scan frequency in rosette, raster, and conventional non-raster scan patterns. The velocities are obtained assuming similar scan area, resolution, and scan time based on the rosette scan parameters, i.e., $R = 3$ μm, $P = 25$ nm, and $T_{scan} = 0.1$ s. Although the maximum tip velocity with the rosette pattern is larger than the one with the raster, cycloid, and CAV spiral, it is still about 36% smaller than that of the Lissajous trajectory. This means that the rosette pattern requires a lower bandwidth for the z-axis nanopositioner to scan the same area at a similar imaging frame rate. We also observe that the tip velocity and reference frequency with rastering are lower than the ones in rosette scanning. However, a high-bandwidth in-plane nanopositioner is required to track a triangular wave at 2127 Hz with sharp apices due to its infinite number of odd harmonics. The presented nonraster scan methods, although demonstrating a lower tip velocity, suffer from other drawbacks such as tip velocity fluctuations and noncontinuous sequential imaging.

In the rosette pattern, the curvilinear rhombi located on the central concentric circles have equal length sides which vary as we move away to either side of these circles.[25] In addition, the length of the diagonals of rhombi alters based on the radii of concentric circles. With a large number of petals, the number of concentric circles increases and most of the rhombi have equal length sides and diagonals. In this case, the diagonals can be considered as the tangential and radial distances as the curvilinear rhombi resemble flat diamonds. To describe how the shape of a curvilinear rhombus changes in the pattern while moving through the concentric circles from periphery to the origin, we define the ratio of tangential distance (TD) to the radial distance (RD) as

$$\alpha_i = \frac{TD_i}{RD_i}, \qquad i \in \{1, 2, \ldots, N\}. \tag{12}$$

Since TD and RD change oppositely from the origin to the periphery, α_i varies in the pattern in accordance with the concentric circles. As demonstrated in Fig. 6, the rhombi have similar shapes on the majority of concentric circles as α_i/α_{i+1} remains almost unity on these circles.

C. Design procedure for rosette scanning

In high-speed AFM imaging, the frame rate and resolution are the key parameters of the scan pattern. Here, the following design
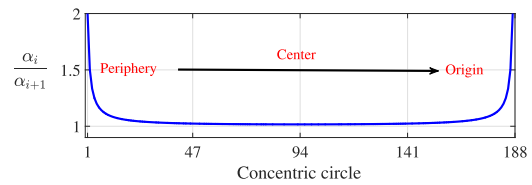
FIG. 6. Ratio of aspect ratios with respect to the concentric circles in a rosette pattern when $R = 3$ μm, $P = 25$ nm, and the scan time is 0.1 s.

procedure is proposed to generate a rosette pattern based on a given scan area, resolution and imaging frame rate:

1. Assuming R is the radius of the circular-shaped scan window, the amplitude of the reference sinusoids is $R/2$.
2. For a desired scan resolution, the integer N is obtained from Eq. (9) by rounding $\frac{R\pi}{2P}$ to the nearest even integer. Then, n is calculated from Eq. (2).
3. Knowing the imaging frame rate or the scan period T, the fundamental scan frequency f is obtained from Eq. (5).
4. Finally, having the fundamental frequency and the rational number n, the reference frequencies f_1 and f_2 are determined from Eq. (4).

Remark. The sampling frequency for imaging should be large enough to ensure that the distance between two data points located on the same scan line is much smaller than the selected resolution in the pattern. Assuming P is the resolution, f_s is the minimum sampling frequency, and v_{max} is the maximum in-plane tip velocity in the rosette pattern, the sampling frequency should meet the following criterion:

$$f_s \geq \frac{v_{max}}{P} = 4fN. \tag{13}$$

Accordingly, the data acquisition device should capture data as fast as f_s, so as the image resolution in Eq. (9) to be still valid.

III. EXPERIMENTS

We performed experiments in closed loop to generate sequential AFM imaging at 10 fps. In all experiments, a dSPACE rapid prototyping system running at a sampling frequency of 90 480 Hz is employed to generate the reference signals and implement the tracking controllers. We design the pattern to allow for a scan radius of $R = 3$ μm and a resolution of $P = 25$ nm. According to Eq. (9), N is obtained as 188. The reference frequencies for both in-plane axes corresponding to this frame rate are 3770 Hz and 10 Hz.

A. MEMS nanopositioner

A 2-DOF MEMS nanopositioner is used to implement the rosette scanning. The device is fabricated using the MEMSCap's SOIMUMP process, and it comprises electrostatic actuators for lateral positioning and bulk piezoresistive sensors to measure the displacement of the scan table, as depicted in Fig. 7. For further details, the readers are referred to Refs. 19 and 26. As shown in Fig. 7, gold features with the thickness of 520 nm are fabricated on the scan table. These features are later used as reference patterns for AFM imaging experiments. The measurement resolution of the piezoresistive
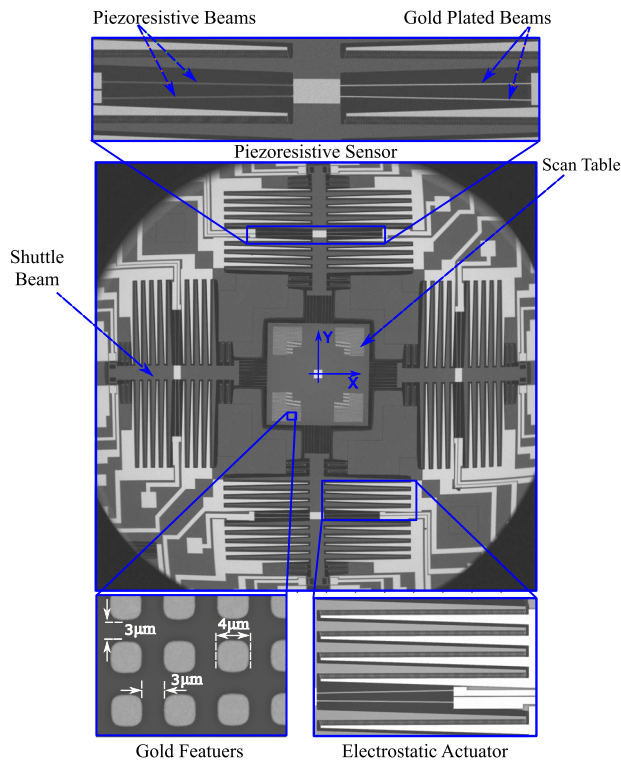
FIG. 7. SEM image of the MEMS nanopositioner. The close-up views show different components of the device. The scan table at the center has the dimensions of 1.8 mm × 1.8 mm. The dimensions of the square-shaped gold patterns on the stage are also shown in the close-up view.

sensors is previously demonstrated to be about 2 nm within the sensing bandwidth of 30 kHz.[14]

The characterization of the nanopositioner is performed using a Polytec MSA-100-3D Micro System Analyzer (MSA). The nanopositioner shows a first resonance frequency of 3538 Hz and 3559 Hz along the x and y axes, respectively.

The displacement range of the nanopositioner is about 15 μm. In the experiments, however, the stroke is limited to 10.70 μm and 10.65 μm along x and y axes, respectively, to stay within a more linear range. By simultaneously recording the sensors' output, calibration factors of 0.219 V/μm and 0.222 V/μm are obtained for x and y sensors, respectively.

The device shows a lightly damped behavior along both axes, making the system prone to external disturbances and vibrations. Therefore, the damping controller previously proposed in Refs. 10 and 27 is also implemented for both axes as shown in Fig. 8. By implementing the damping controller, the 2% settling time of the system is decreased to less than 0.5 ms, while the 3 dB-bandwidth of the device is also improved to 4.5 kHz along both directions. The tracking controller is designed for the damped nanopositioner as explained next.

B. Internal-model-based controller

The internal-model-based controller is an effective method for tracking reference signals with known dynamics.[28] According to the
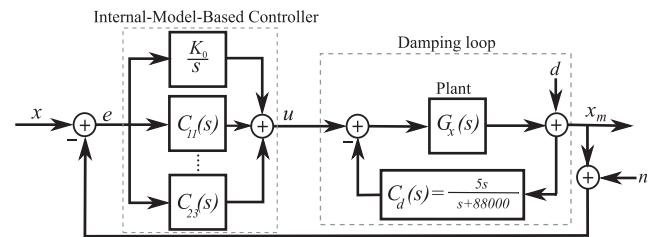

FIG. 8. Block diagram of the closed-loop system in the x axis. The same scheme is used in the y axis.

internal model principle, if the controller incorporates the reference generating polynomial, the system can robustly track the reference signals.[28] Furthermore, the steady state tracking error asymptotically approaches zero when the internal model of the reference signal and deterministic disturbances are included in the controller.[29] Here, the reference signals are pure sinusoids; hence, the internal-model-based controller can improve the tracking performance by including the reference harmonics. This controller also restricts the closed-loop bandwidth, preventing the projected sensor noise from affecting the tracking performance of the nanopositioner.[30] As previously discussed in Ref. 14, to reject the undesirable harmonics appearing in the tracking error due to system nonlinearities, we design the controllers to incorporate pure imaginary poles corresponding to the reference frequencies and their harmonics. This leads to the following controller:

$$C(s) = \frac{K_0}{s} + \sum_{\ell=1}^{2} C_{1\ell}(s) + \sum_{p=1}^{3} C_{2p}(s), \tag{14}$$

where

$$C_{1\ell}(s) = K_{1\ell} \frac{s - z_{1\ell}}{s^2 + (\ell\omega_1)^2},$$
$$C_{2p}(s) = K_{2p} \frac{s - z_{2p}}{s^2 + (p\omega_2)^2}. \tag{15}$$

A schematic of the x-axis closed-loop system incorporating this controller is depicted in Fig. 8. The same control scheme is also applied to the y axis. Controller zeros at each reference frequency are empirically adjusted to achieve high performance tracking. Furthermore, controller gains are tuned to provide stability margins of approximately 16.6 dB and −81.5° for the x axis and 17.5 dB and 82.3° for the y axis. It is worth noting that the internal model of the third harmonic of f_1 is not included in the controllers. The primary reason being that the third harmonic is beyond the bandwidth of the damped system at higher frame rates and its effect becomes insignificant in the tracking error due to the system frequency response roll-off. In addition, including more harmonics in the controller will increase its order, making its real-time implementation challenging.

C. Experimental results

We performed tracking experiments in a closed loop with the internal-model-based controllers described above. As illustrated in Figs. 9(a) and 9(b), the lateral axes of the nanopositioner accurately track the reference signals. The close-up views of the x and y tracking
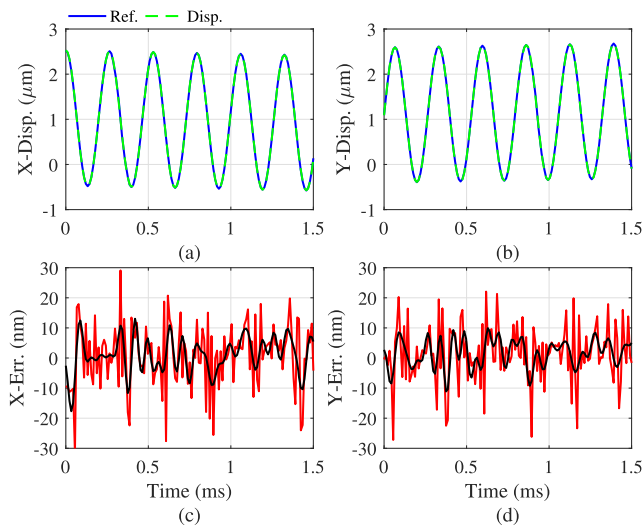
FIG. 9. Close-up views of reference signals and displacement in (a) x and (b) y axes. $R = 3$ μm, $P = 25$ nm, and the frame rate is 10 fps. Close-up views of the tracking error in (c) x and (d) y axes. Red curves show the actual error, and black curves are the filtered error.
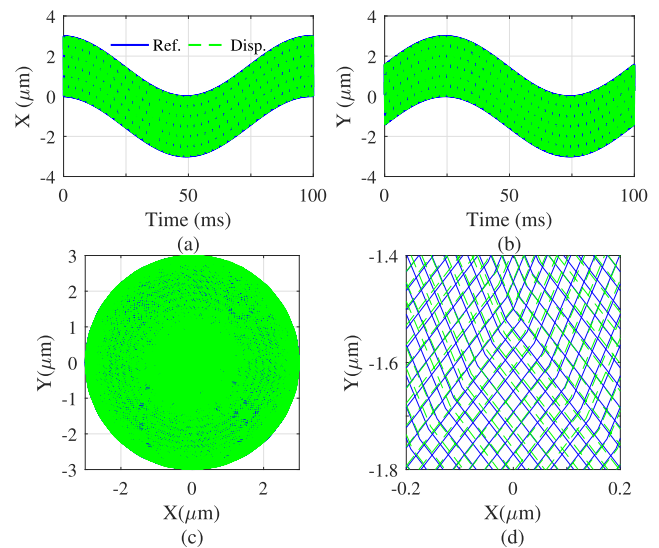

FIG. 10. Reference signal and displacement in one scan interval in (a) x and (b) y axes. $R = 3$ μm, $P = 25$ nm, and the frame rate is set to 10 fps. (c) Reference and actual trajectory. (d) Close-up view of the reference and actual trajectory.

errors in Figs. 9(c) and 9(d) reveal the efficacy of incorporating the internal modes of the reference signals and their harmonics in the controller.

The tracking error contains stochastic and deterministic components. In this work, the deterministic component appearing as harmonics in tracking error is minimized using the internal-model-based controller. Amplifier noise, sensor noise, and external disturbances all contribute to the stochastic component of the stage tracking error. We attempted to minimize the last two sources of stochastic noise by performing the experiments in a closed metal box and on an optical table.

As depicted in Fig. 8, the sensor noise is fed back to the system appearing as the projected noise at the stage displacement output. During the control design, this projected noise is minimized by using a damping controller with a high-pass profile as well as using a tracking controller with a limited bandwidth. For instance, the closed-loop bandwidth of the tracking controller at 10 fps is approximately 1 Hz. The high-pass damping loop reduces the effect of $1/f$ noise inherent to the piezoresistive sensors.[26]

The sensor data are filtered using a Kaiser window low-pass filter with a cut-off frequency of 15 kHz and a stop band attenuation of 60 dB. Figures 9(c) and 9(d) show the filtered error in each axis. The reference and actual trajectories obtained from the filtered sensor data for one scan period are depicted in Fig. 10(c). The close-up view of the actual position and the reference trajectory in Fig. 10(d) clearly shows that the scan lines precisely follow the rosette pattern.

The root mean square (rms) values of the original and filtered tracking errors at 10 fps along with the percent error with respect to the scan diameter are stated in Table II. The rms values indicate that the system satisfactorily tracks the reference signal owing to the internal-model-based controller. The peak to peak value of tracking

error in both axes is calculated to be about 20 nm, which is obtained at the $\pm 2\sigma$ level. This measure is reliable with 95.4% certainty, considering a normal distribution of the tracking error. Note that the images are generated based on the sensor data not the reference signals. Hence, the tracking error will not be reflected into the image. However, if the error exceeds the pattern resolution, the trajectory will be slightly distorted and the tracking error will determine the actual resolution of the image.

D. Sequential AFM imaging

To evaluate the performance of the closed-loop positioning system with the rosette pattern, we acquired a series of AFM images at the high frame rate of 10 fps. For this purpose, we used the MEMS nanopositioner described above as the scan stage mounted within an AFMWorkshop TT-AFM. Figure 11 shows the experimental setup including the AFM, the MEMS nanopositioner, and a printed circuit board (PCB) which provides the sensing and actuation signal paths. A series of periodic gold patterns with the dimensions of $4 \times 4 \times 0.5$ μm^3 fabricated on the stage were utilized as scan samples. To construct 3D images, the cantilever deflection

TABLE II. Closed-loop rms tracking errors in x and y axes and the error percentage with respect to the scan diameter at 10 fps.

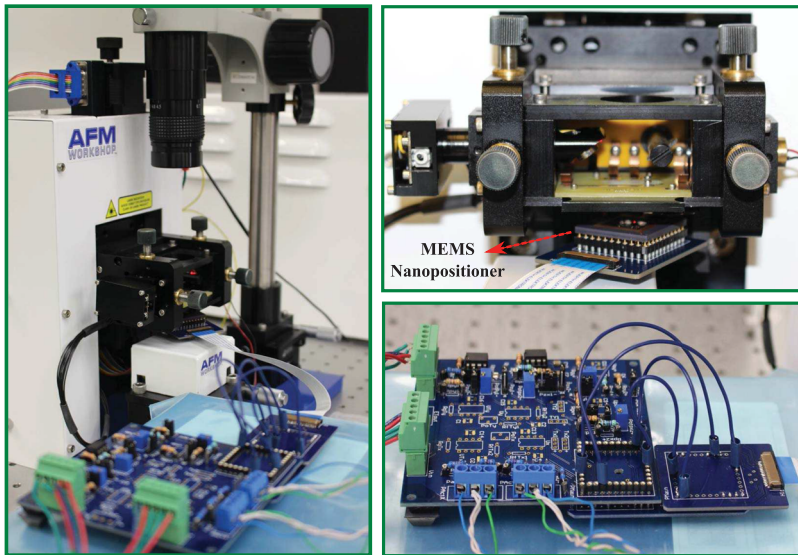|	Original		Filtered	
	(nm)	(%)	(nm)	(%)
X	9.43	0.15	5.10	0.09
Y	8.78	0.16	4.93	0.08

FIG. 11. Experimental setup for AFM imaging using the MEMS nanopositioner.

provided by the AFM built-in optical beam detector and in-plane displacement from the nanopositioner piezoresistive sensors were simultaneously recorded. Due to the low-bandwidth nature of the AFM z-axis positioner, the imaging was performed in constant-height contact mode. Therefore, a contact-mode cantilever was employed with a resonance frequency of 20.8 kHz and a stiffness of approximately 0.19 N/m.

In all experiments, initially, the amplitude of x and y sinusoids was gradually increased from zero to the maximum displacement corresponding to the scan window radius. Then, imaging was performed using the rosette pattern, while the MEMS nanopositioner was slowly moved in the x-y plane by implementing the raster scanning with the embedded positioner of the TT-AFM at a low frequency of 0.1 Hz. Therefore, the moving features could be observed during AFM imaging. Figure 12 illustrates a series of AFM images obtained at 10 fps while the slowly moving gold feature is observable in the image. Since the scanning is performed in constant-height contact mode, the AFM cantilever vibrates as it experiences sharp transitions at high frame rates. Therefore, some artifacts appear in the AFM image and degrade its quality. Operating the AFM in the constant-force mode will address this issue. That, however, would require a z-axis positioner with a very high bandwidth that was not available at the time these experiments were performed.
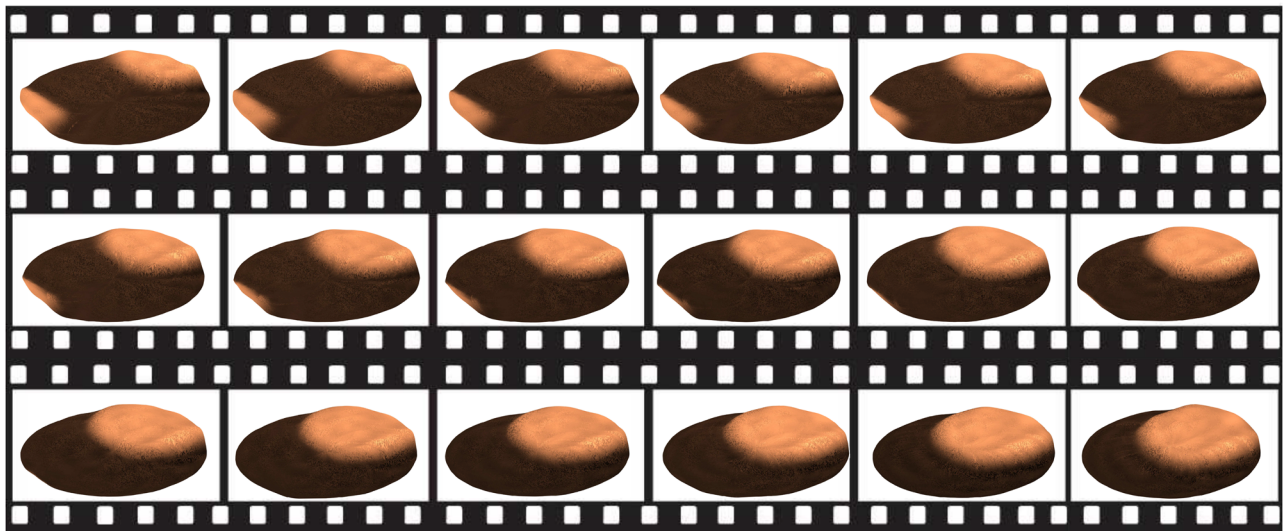

FIG. 12. A series of video frames (from top-left to bottom-right) of a slowly moving sample. Each frame was captured at 0.1 s equivalent to a video-rate of 10 fps to scan a circular-shaped area with the diameter of 6 μm by using a commercial AFM operating in a constant-height contact mode.

IV. CONCLUSION

We proposed a novel nonraster scan pattern for high-speed AFM imaging. We analyzed the pattern mathematically to derive a closed-form formula for the scan resolution and determine the scan parameters according to the scan size and imaging frame rate. Since the reference signals are a sum of pure sinusoids with constant amplitude and frequency, tracking of this pattern is straightforward. We employed an internal-model-based controller that incorporates the dynamics of the reference signals and undesirable harmonics to achieve high performance results at 10 fps. This method was satisfactorily implemented using a commercial AFM and a MEMS nanopositioner as the scanning stage, and a sequence of images was acquired with an AFM operating in the constant-height contact mode. Since the pattern is periodic, the nanopositioner can traverse the scan area many times repeatedly without the need for a high-bandwidth tracking controller. Consequently, the rosette pattern is appropriate for sequential AFM imaging to interrogate dynamic samples at the nanoscale.

APPENDIX A: THE SCAN PERIOD

If p and q are periods of $f(x)$ and $g(x)$, respectively, then, any common multiple of p and q is a period of $f(x) + g(x)$. Hence, the least common multiple (LCM) of p and q, if it exists, is a period of $f(x) + g(x)$. According to this principle, the period of the reference signals in Eq. (3), i.e., T_x and T_y, can be obtained as

$$T_x = T_y = \text{LCM}\left\{\frac{1}{f(1+n)}, \frac{1}{f(1-n)}\right\}. \tag{A1}$$

By substituting n from Eq. (2), the period of x, y, and the resulting pattern is obtained as follows:

$$T = T_x = T_y = \text{LCM}\left\{\frac{N+1}{f(2N+1)}, \frac{N+1}{f}\right\} = \frac{N+1}{f}. \tag{A2}$$

APPENDIX B: THE NUMBER OF PETALS

As depicted in Fig. 2, a petal is a part of the rosette pattern surrounding its origin. The petals copy themselves to create a circular-shaped rosette pattern. The number of petals is related to the value of n in Eq. (2). To determine the number of petals, we obtain the duration of time required for a petal to be plotted and then divide it by the total scan time for the rosette pattern. According to Eq. (1), $r = R\cos(n\theta)$ in the polar coordinate system. Based on the definition used here, each petal starts and ends at $r = 0$, which happens at the following polar angles:

$$\theta_k = \frac{(2k+1)\pi}{2n}. \tag{B1}$$

Considering $\theta = 2\pi ft$, the difference between two consecutive θ_k determines the duration wherein a petal is drawn, i.e.,

$$t_p = \frac{1}{2nf}. \tag{B2}$$

Thus, using Eqs. (2) and (5), the number of petals in one scan time is

$$\text{Number of Petals} = \frac{T}{t_p} = 2N. \tag{B3}$$

APPENDIX C: THE SCAN RESOLUTION

For high resolution rosette scanning, a curvilinear rhombus resembles a flat diamond; hence, the distance between two adjacent scan lines is the altitude of the rhombus as shown in Fig. 13(a). Therefore, the resolution corresponds to the altitude of rhombi with the largest area.

The area of a rhombus, $A : \mathbb{N} \rightarrow \mathbb{R}$, can be obtained as

$$A(k) = \frac{\text{TD}_k \times \text{RD}_k}{2}, \qquad k = 1, \ldots, N, \tag{C1}$$

where k denotes the kth concentric circle. Assuming A to be affine on each interval $[k, k+1]$, we have

$$A(k+1) + A(k-1) - 2A(k)$$
$$= \frac{-4\pi R^2}{N}\sin\left(\frac{\pi}{2N+2}\right)\sin\left(\frac{(2k+1)\pi}{2N+2}\right) < 0, \qquad k = 1, \ldots, N, \tag{C2}$$
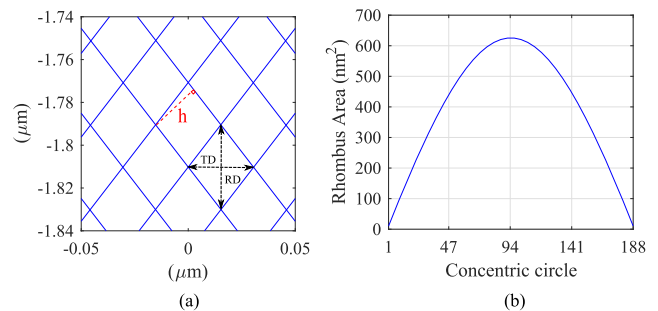

FIG. 13. (a) Close-up view of the rosette pattern around the central concentric circles. (b) Profile of rhombus area corresponding to the concentric circles in the pattern when $R = 3\ \mu$m, $P = 25$ nm, and the frame rate is 10 fps.

which proves that A is concave as depicted in Fig. 13(b). To obtain the largest area with no data point inside, the maximum of A is acquired at $k^* = (N + 1)/2$ by solving $A(k) - A(k - 1) = 0$. As is also visible in Fig. 13(b), the closest integer solutions to k^* are $\{(N/2), (N/2) + 1\}$, representing the two central concentric circles on which the maximum area occurs. For large values of N, RD and TD at k^* can be obtained using Eq. (8) as follows:

$$\text{RD}^* \approx \text{TD}^* \approx \frac{\sqrt{2}}{2} \frac{R\pi}{N}. \tag{C3}$$

According to Fig. 13(a), the altitude of a rhombus is

$$h = \frac{\text{TD} \times \text{RD}}{2\sqrt{\left(\frac{\text{TD}}{2}\right)^2 + \left(\frac{\text{RD}}{2}\right)^2}}, \tag{C4}$$

and by substituting Eq. (C3) into Eq. (C4), the resolution is approximated by

$$P \approx \frac{R\pi}{2N}. \tag{C5}$$

REFERENCES

[1] T. Ando, "High-speed atomic force microscopy and its future prospects," Biophys. Rev. **10**, 285–292 (2018).

[2] S. Deville, J. Chevalier, G. Fantozzi, R. Torrecillas, J. F. Bartolomé, and J. S. Moya, "Atomic force microscopy study of the surface degradation mechanisms of zirconia based ceramics," preprint arXiv:1804.00002 (2018).

[3] A. Trache, L. Xie, H. Huang, V. V. Glinsky, and G. A. Meininger, "Applications of atomic force microscopy for adhesion force measurements in mechanotransduction," in *Nanoscale Imaging* (Springer, 2018), pp. 515–528.

[4] N. Pavliček and L. Gross, "Generation, manipulation and characterization of molecules by atomic force microscopy," Nat. Rev. Chem. **1**, 5 (2017).

[5] Y. K. Yong, S. O. R. Moheimani, B. J. Kenton, and K. Leang, "Invited review article: High-speed flexure-guided nanopositioning: Mechanical design and control issues," Rev. Sci. Instrum. **83**, 121101 (2012).

[6] S. O. R. Moheimani, "Invited review article: Accurate and fast nanopositioning with piezoelectric tube scanners: Emerging trends and future challenges," Rev. Sci. Instrum. **79**, 071101 (2008).

[7] A. J. Fleming and A. G. Wills, "Optimal periodic trajectories for band-limited systems," IEEE Trans. Control Syst. Technol. **17**, 552–562 (2009).

[8] I. A. Mahmood, S. O. R. Moheimani, and B. Bhikkaji, "A new scanning method for fast atomic force microscopy," IEEE Trans. Nanotechnol. **10**, 203–216 (2011).

[9] A. Bazaei, M. Maroufi, A. G. Fowler, and S. O. R. Moheimani, "Internal model control for spiral trajectory tracking with MEMS AFM scanners," IEEE Trans. Control Syst. Technol. **24**, 1717–1728 (2016).

[10] A. Bazaei, M. Maroufi, and S. O. R. Moheimani, "Tracking control of constant-linear-velocity spiral reference by LQG method," IFAC-PapersOnLine **50**, 15568–15573 (2017).

[11] A. Bazaei, Y. K. Yong, and S. O. R. Moheimani, "High-speed Lissajous-scan atomic force microscopy: Scan pattern planning and control design issues," Rev. Sci. Instrum. **83**, 063701 (2012).

[12] T. Tuma, J. Lygeros, V. Kartik, A. Sebastian, and A. Pantazi, "High-speed multiresolution scanning probe microscopy based on Lissajous scan trajectories," Nanotechnology **23**, 185501 (2012).

[13] Y. K. Yong, S. O. R. Moheimani, and I. Petersen, "High-speed cycloid-scan atomic force microscopy," Nanotechnology **21**, 365503 (2010).

[14] N. Nikooienejad, A. Alipour, M. Maroufi, and S. O. R. Moheimani, "Video-rate non-raster AFM imaging with cycloid trajectory," IEEE Trans. Control Syst. Technol. (to be published).

[15] B. Bhikkaji, M. Ratnam, A. J. Fleming, and S. O. R. Moheimani, "High-performance control of piezoelectric tube scanners," IEEE Trans. Control Syst. Technol. **15**, 853–866 (2007).

[16] D. Ziegler, T. R. Meyer, A. Amrein, A. L. Bertozzi, and P. D. Ashby, "Ideal scan path for high-speed atomic force microscopy," IEEE/ASME Trans. Mech. **22**, 381–391 (2017).

[17] B. Hartman and S. B. Andersson, "Feature tracking for high speed AFM imaging of biopolymers," Int. J. Mol. Sci. **19**, 1044 (2018).

[18] T. R. Meyer, D. Ziegler, C. Brune, A. Chen, R. Farnham, N. Huynh, J.-M. Chang, A. L. Bertozzi, and P. D. Ashby, "Height drift correction in non-raster atomic force microscopy," Ultramicroscopy **137**, 48–54 (2014).

[19] M. Maroufi and S. O. R. Moheimani, "A 2DOF SOI-MEMS nanopositioner with tilted flexure bulk piezoresistive displacement sensors," IEEE Sens. J. **16**, 1908–1917 (2016).

[20] M. Pawley, "Closed plane curves described by finite and infinite sums of rotating vectors," J. Franklin Inst. **307**, 155–173 (1979).

[21] L. M. Hall, "Trochoids, roses, and thorns beyond the spirograph," Coll. Math. J. **23**, 20–35 (1992).

[22] N. Nikooienejad, M. Maroufi, and S. O. R. Moheimani, "A novel non-raster scan method for AFM imaging," in *ASME 2018 Dynamic Systems and Control Conference* (American Society of Mechanical Engineers, 2018).

[23] P. Huang and S. B. Andersson, "Generating images from non-raster data in AFM," in *Proceedings of the 2011 American Control Conference* (IEEE, 2011), pp. 2246–2251.

[24] Y. R. Teo, Y. K. Yong, and A. J. Fleming, "A comparison of scanning methods and the vertical control implications for scanning probe microscopy," Asian J. Control **20**, 1352–1366 (2018).

[25] P. Rosin, "Rosettes and other arrangements of circles," Nexus Network J. **3**, 113–126 (2001).

[26] M. Maroufi, A. Bazaei, A. Mohammadi, and S. O. R. Moheimani, "Tilted beam piezoresistive displacement sensor: Design, modeling, and characterization," J. Microelectromech. Syst. **24**, 1594 (2015).

[27] M. G. Ruppert, M. Maroufi, A. Bazaei, and S. O. R. Moheimani, "Kalman filter enabled high-speed control of a MEMS nanopositioner," IFAC-PapersOnLine **50**, 15554–15560 (2017).

[28] G. C. Goodwin, S. F. Graebe, and M. E. Salgado, *Control System Design* (Prentice Hall, Upper Saddle River, 2001), p. 13.

[29] B. A. Francis and W. M. Wonham, "The internal model principle of control theory," Automatica **12**, 457–465 (1976).

[30] M. Maroufi, A. Bazaei, and S. O. R. Moheimani, "A high-bandwidth MEMS nanopositioner for on-chip AFM: Design, characterization, and control," IEEE Trans. Control Syst. Technol. **23**, 504–512 (2015).